Monthly Notices
of the
ROYAL ASTRONOMICAL SOCIETY

Mon. Not. R. Astron. Soc. **425,** 1781–1788 (2012) doi:10.1111/j.1365-2966.2012.20878.x

A new layout optimization technique for interferometric arrays, applied to the Murchison Widefield Array

A. P. Beardsley,[1] B. J. Hazelton,[1] M. F. Morales,[1⋆] R. J. Capallo,[2] R. Goeke,[3] D. Emrich,[4] C. J. Lonsdale,[2] W. Arcus,[4] D. Barnes,[5] G. Bernardi,[6] J. D. Bowman,[7] J. D. Bunton,[8] B. E. Corey,[2] A. Deshpande,[9] L. deSouza,[8,10] B. M. Gaensler,[10,11] L. J. Greenhill,[6] D. Herne,[4] J. N. Hewitt,[3] D. L. Kaplan,[12] J. C. Kasper,[6] B. B. Kincaid,[2] R. Koenig,[8] E. Kratzenberg,[2] M. J. Lynch,[4] S. R. McWhirter,[2] D. A. Mitchell,[6,11] E. Morgan,[3] D. Oberoi,[2] S. M. Ord,[6] J. Pathikulangara,[8] T. Prabu,[9] R. A. Remillard,[3] A. E. E. Rogers,[2] A. Roshi,[9] J. E. Salah,[2] R. J. Sault,[13] N. Udaya Shankar,[9] K. S. Srivani,[9] J. Stevens,[8,14] R. Subrahmanyan,[9] S. J. Tingay,[4,11] R. B. Wayth,[4,6] M. Waterson,[4,15] R. L. Webster,[11,13] A. R. Whitney,[2] A. Williams[16,17] C. L. Williams[3] and J. S. B. Wyithe[11,13]

[1] *University of Washington, Department of Physics, Seattle, WA 98195, USA*
[2] *MIT Haystack Observatory, Westford, MA 01886, USA*
[3] *MIT Kavli Institute for Astrophysics and Space Research, Cambridge, MA 02139, USA*
[4] *International Centre for Radio Astronomy Research, Curtin University, Perth, WA 6845, Australia*
[5] *Centre for Astrophysics and Supercomputing, Swinburne University of Technology, Hawthorn, VIC 3122, Australia*
[6] *Harvard-Smithsonian Center for Astrophysics, Cambridge, MA 02138, USA*
[7] *Arizona State University, School of Earth and Space Exploration, Tempe, AZ 85287, USA*
[8] *CSIRO Astronomy and Space Science, Epping, NSW 1710, Australia*
[9] *Raman Research Institute, Bangalore, 560080, India*
[10] *The University of Sydney, School of Physics, NSW 2006, Australia*
[11] *ARC Centre of Excellence for All-Sky Astrophysics (CAASTRO), The University of Sydney, NSW 2006, Australia*
[12] *University of Wisconsin–Milwaukee, Department of Physics, Milwaukee, WI 53201, USA*
[13] *The University of Melbourne, School of Physics, Parkville, VIC 3010, Australia*
[14] *University of Tasmania, Hobart, TAS 7001, Australia*
[15] *The Australian National University, Weston Creek, ACT 2611, Australia*
[16] *Perth Observatory, Bickley, WA 6076, Australia*
[17] *The University of Western Australia, Nedlands, WA 6009, Australia*

Accepted 2012 March 5. Received 2012 February 27; in original form 2011 September 6

ABSTRACT

Antenna layout is an important design consideration for radio interferometers because it determines the quality of the snapshot point spread function (PSF, or array beam). This is particularly true for experiments targeting the 21-cm Epoch of Reionization signal as the quality of the foreground subtraction depends directly on the spatial dynamic range and thus the smoothness of the baseline distribution. Nearly all sites have constraints on where antennas can be placed – even at the remote Australian location of the Murchison Widefield Array (MWA) there are rock outcrops, flood zones, heritages areas, emergency runways and trees. These exclusion areas can introduce spatial structure into the baseline distribution that enhances the PSF sidelobes and reduces the angular dynamic range. In this paper we present a new method of constrained antenna placement that reduces the spatial structure in the baseline distribution.

⋆E-mail: mmorales@phys.washington.edu

This method not only outperforms random placement algorithms that avoid exclusion zones, but surprisingly outperforms random placement algorithms without constraints to provide what we believe are the smoothest constrained baseline distributions developed to date. We use our new algorithm to determine antenna placements for the originally planned MWA, and present the antenna locations, baseline distribution and snapshot PSF for this array choice.

Key words: instrumentation: interferometers – cosmology: miscellaneous.

1 INTRODUCTION

Antenna placement is a critical design criterion for any interferometric array as it determines the baseline distribution and thus the angular distribution of the point spread function (PSF) of the radio telescope. Nearly all observatory sites have areas where antennas cannot be placed. Buildings, roads, runways, power and data access, land use and ownership issues, endangered flora and fauna, flood zones, elevation, and ground stability are but a few of the common issues that constrain the placement of antennas. Even in remote desert locations, a flat and barren terrain can quickly become dotted with exclusion zones where antennas cannot be placed.

This is of particular concern for 21-cm Cosmology telescopes targeting the Epoch of Reionization (EoR) and baryon acoustic oscillation dark energy measurements, as the quality of the monochromatic PSF is directly related to the ability to subtract foreground contamination (Morales, Bowman & Hewitt 2006; Bernardi et al. 2011; Datta, Bowman & Carilli 2011; Liu & Tegmark 2011; Vedantham, Shankar, Subrahmanyan 2012). Antenna exclusion zones can introduce asymmetries in the baseline distribution which limit the angular dynamic range and thus achievable level of foreground subtraction (see Morales & Wyithe 2010 for a recent review of foreground subtraction for 21-cm Cosmology).

There is a long history of array configuration studies, including optimization of arrays with cost constraints (e.g. Cohanim, Hewitt & Weck 2010), simulated annealing for small N arrays (Cornwell 1988), optimization to reduce the peak sidelobe levels [Kogan 2000; Kogan & Cohen 2005, Long Wavelength Array (LWA) Memo 21] or optimization to match a particular baseline distribution with and without ground constraints (Boone 2001, Lal et al. SKA Memo 107). Our particular concern is situations in which some areas cannot be used (exclusion zones), a particular radial baseline distribution must be met and a very high angular dynamic range must be achieved. While our problem is similar to that of Boone (2001), we find that the figure of merit used in that work does not sufficiently capture large-scale structure in the baseline distribution. We develop an alternative figure of merit, which naturally leads to a new optimization method.

In Section 2 we explore the effect of exclusion zones on the baseline distribution, develop a new spatially sensitive figure of merit and present our new optimization method. We then apply our method to placing the Murchison Widefield Array (MWA) antennas in Section 3, and present a 512-antenna layout for the MWA. The as-funded MWA will consist of a 128 antenna subset of this layout, described elsewhere (Tingay et al. 2012). The locations of all 512 antennas are provided electronically (Table A1, see Supporting Information).

2 ARRAY LAYOUT COMPARISONS AND A NEW TECHNIQUE

Proposed and future large N radio arrays will face the challenge of placing hundreds to thousands of antennas to optimize scientific goals, while obeying numerous constraints. While most physical constraints exist on the antenna locations (areas of exclusion on the ground), science capabilities are optimized in the uv plane for an interferometric measurement, and hence these arrays should match the ideal *baseline* distribution as closely as possible. This makes the problem very non-linear because any one antenna placement affects $N - 1$ baselines, and it is not immediately obvious how a constraint such as an exclusion area will affect the baseline distribution.

In our analysis, we explored three array layout methods. The first method is random and with no exclusion areas ('random unmasked'), in which antennas are placed randomly with a weighted radial distribution. Algorithmically, for each antenna a radius is first drawn from a distribution that matches the desired radial density profile, then azimuthal angles are chosen at random until one is found that does not overlap with previously placed antennas. The second array generation method is also random but incorporates exclusion areas ('random masked'). This method is identical to the random unmasked method, with the addition of avoiding exclusion areas by the use of a mask that is checked in the same step as checking for overlap with previous antennas. The third and final method is the algorithm that we developed ('active method'), which actively minimizes spatial structure in the baseline distribution and is detailed later in this section.

We assume that the scientifically desired uv or antenna distribution of the array is known. For our examples we use the specifications for the original MWA telescope which has a dense core optimized for EoR measurements, with a smooth radial dependence. More details of the MWA distribution are given in Section 3, but for a full motivation, see Bowman, Morales & Hewitt (2006). While we use this example for our work, our methods are generalizable to any large N array.

Fig. 1 shows three examples of baseline distributions generated by the random unmasked, random masked and active masked methods, respectively. The left-hand panel shows the baseline distribution on a logarithmic scale, while the right-hand panel shows the difference from the ideal smooth analytic function to accentuate undesired structures in the uv distributions. These three examples are representative of the over 4000 array layouts we have hand graded to arrive at our conclusions.

All of these images have fuzzy small-scale noise due to the finite number of antennas. However, there is another more insidious artefact present in the masked baseline distribution (middle row of Fig. 1) – large-scale structure imprinted by the antenna exclusion areas. In all of the masked random array realizations there are significant regions of over- and underdensities in the baseline distribution which translate directly into unwanted PSF features.

To understand the effect of baseline over- and underdensities, consider a nearly perfect uv distribution with a small region of excess baselines. This region of uv overdensity can be viewed as a 'wave packet' of baselines at similar spatial frequencies. In the wave packet picture, there is a fundamental corrugation in the PSF given by the location of the centre of the excess region. However,

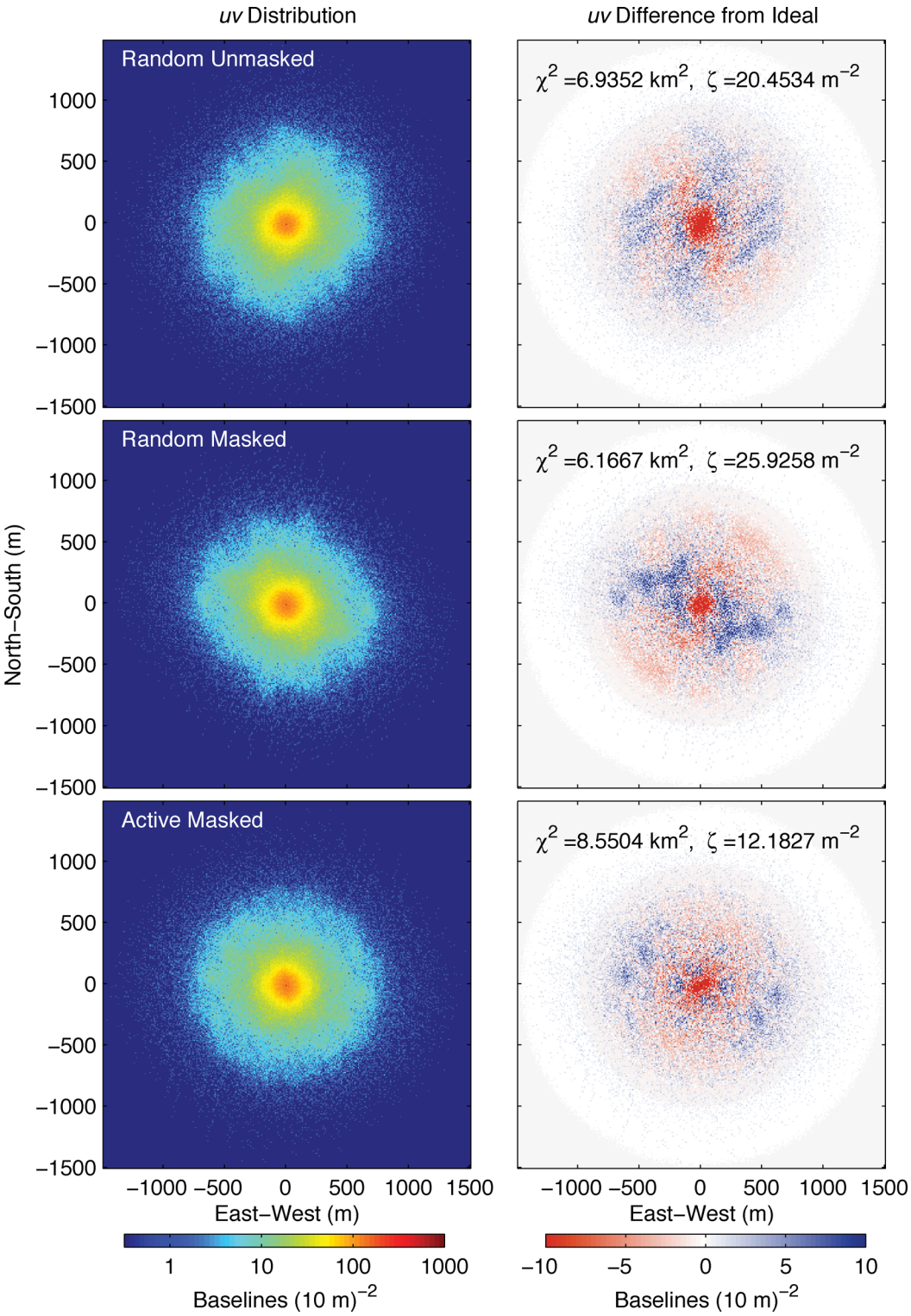

Figure 1. Example *uv* distributions for array layouts generated by (top to bottom) the random unmasked, random masked and active masked methods. The left-hand panels show the snapshot single-frequency baseline distributions on a log scale, while the right-hand panels show the difference of this distribution from the smooth analytic ideal. The small-scale fuzzy noise is equally present in all array realizations and is due to the finite number of antennas. However, the large-scale structure varies greatly from array to array. The exclusion areas have introduced significant asymmetries in the baseline distribution of the random masked method (middle row). The active masked method (bottom row) is able to highly suppress this structure, even beyond the level of the *unconstrained* random method (top row). Furthermore, we see that the χ^2 values for these sample arrays show no correlation with the quality of the arrays; however, the figure of merit, ζ, accurately reflects the amount of azimuthal structure in the distributions (see Fig. 2).

the nearby modes in the packet beat in and out of phase with the fundamental corrugation. When the wavenumbers are all in phase, the amplitude is very high – the number of excess baselines in the region – but they quickly dephase only to rephase again some distance further along in the PSF. The undesirable 'features' seen in most PSFs are the periodic signature of a wave packet beating across the PSF. Over- (or under-)dense regions that cover a large portion of the *uv* plane will quickly damp down (wide bandwidth), though they often have a lot of power due to the large number of baselines involved, and correspond to large close-in sidelobes. Smaller features in the *uv* plane damp more slowly and repeat many times across the PSF, leading to the small far sidelobes. A smooth *uv* distribution necessarily leads to a smooth PSF, and the PSF sidelobe structure is dominated not by the unavoidable fuzzy noise but instead by the larger regions of over- and underdensity in the *uv* plane.

Our first approach to quantify the deviations from the desired *uv* distributions was to consider χ^2. This was calculated by gridding the *uv* distribution and integrating the square of the difference from the ideal, weighted by the variance in each pixel from 500 random unmasked realizations. However, χ^2 is not a spatially aware function – any deviation from the ideal is weighted the same regardless of where in the *uv* plane the deviation occurs. Because of this lack of spatial information, χ^2 does not capture the large-scale structure that is important for choosing an array. The examples in Fig. 1 vary quite a bit in quality; however, the associated χ^2 values do not reliably reflect the degree of spatial structure. The insensitivity of χ^2 to array quality is demonstrated again in the histogram in the left-hand panel of Fig. 2. Despite a clear qualitative difference between the masked and unmasked random configurations (dashed blue and dash–dotted red), the distributions of χ^2 are very similar.

With the spatial dependence in mind, our next step was to develop a figure of merit based on a Bessel decomposition. The residual *uv* distribution [$D(r, \phi)$, difference between actual and desired] can be decomposed into Bessel modes

$$D(r,\phi) = \sum_{n=1}^{\infty}\sum_{m=0}^{\infty} J_m\left(\frac{x_{mn}r}{R}\right)[A_{mn}\sin(m\phi) + B_{mn}\cos(m\phi)], \quad (1)$$

where x_{mn} is the nth zero of the mth Bessel function and R is the maximum allowed baseline length. Using the orthogonality of the Bessel functions, we can determine A_{mn} and B_{mn} (e.g. Jackson 1999)

$$A_{mn} = \frac{2}{\pi R^2 J_{m+1}^2(x_{mn})}\int_0^{2\pi} \mathrm{d}\phi \int_0^R \mathrm{d}r\, r D(r,\phi) J_m\left(\frac{x_{mn}r}{R}\right)\sin(m\phi), \quad (2a)$$

$$B_{mn} = \frac{2}{\pi R^2 J_{m+1}^2(x_{mn})}\int_0^{2\pi} \mathrm{d}\phi \int_0^R \mathrm{d}r\, r D(r,\phi) J_m\left(\frac{x_{mn}r}{R}\right)\cos(m\phi). \quad (2b)$$

The amplitudes of the asymmetric Bessel coefficients ($A_{mn}, B_{mn}, m > 0$) reflect the asymmetric spatial over- and under-densities in the *uv* plane. We then define a figure of merit ζ as the sum of these Bessel coefficients:

$$\zeta \equiv \sum_{n=1}^{\max(n)}\sum_{m=1}^{\max(m)} \sqrt{A_{mn}^2 + B_{mn}^2}\,. \quad (3)$$

The double sum is not infinite for two reasons: computational time, and higher modes describe smaller scale structure. Because we are interested in suppressing large-scale structure in the *uv*, we can truncate the sum. For our work, we found that values of $\max(n) = 10$ and $\max(m) = 20$ were computationally feasible and provided sufficient information to suppress the large-scale structure.

Smaller ζ corresponds to less spatial structure, and hence a more desirable layout. The right-hand panel of Fig. 2 shows the ζ distributions for the same arrays, clearly separating the masked and unmasked random arrays, and in Fig. 1 the ζ values accurately track the quality of the array realizations.

To minimize our figure of merit, we created an active masked algorithm based on the ζ figure of merit. For computational reasons, we first place a subset of the antennas (350 of 496 for our example) using the random masked method. Then for each remaining antenna, we first choose a weighted random radius, r, and many candidate azimuthal locations (angular spacing of 10 m in our example). We then select the location with the smallest ζ value, and repeat until all N antennas are placed.

The result is clear in Figs 1 and 2. Despite having the additional constraint of the exclusion areas, the active masked method produces more symmetric baseline distributions than either the random

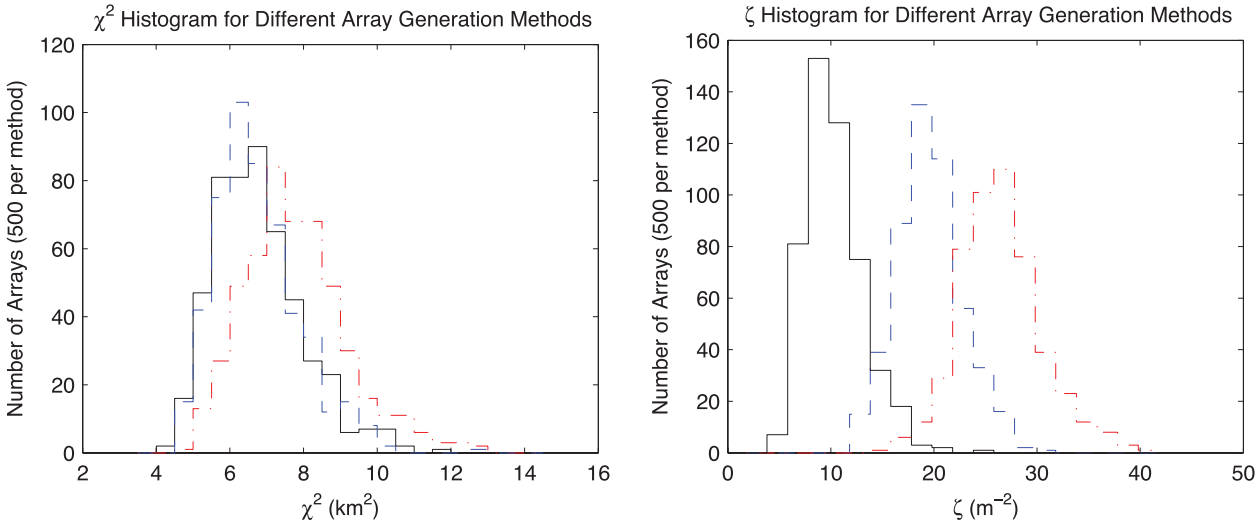

Figure 2. χ^2 and ζ histograms for random unmasked, random masked and active masked methods as denoted by the thick dashed blue, thick dot–dashed red and thin solid black lines, respectively. While the χ^2 values do not distinguish the quality of the different realizations (a conclusion firmly supported by our hand grading), the ζ values strongly separate the realizations based on asymmetry.

masked (expected) or random unmasked methods (unexpected). We can see this qualitatively by comparing the baseline distributions in the three examples. In the thousands of arrays we examined by hand, we observed a very strong correlation between small ζ and spatial symmetry. The success of our algorithm is shown statistically by the distribution of ζ values for the three methods in the right-hand panel of Fig. 2.

It is of interest to note that significant baseline asymmetry arises even in the unmasked random array realizations (Fig. 1, top row, no exclusion areas). These asymmetries are due to shot noise in the random antenna placement. Conceptually, as the last few antennas are added, images of the entire array are added to the *uv* plane at that distance from the centre. For centrally condensed arrays, this can produce lumps in the *uv* plane. Alternatively, one can consider moving a single antenna on the ground which coherently changes $N - 1$ baselines. Small random associations can thus make significant correlations in the baseline distribution.

The new active method based on the Bessel decomposition figure of merit produces arrays which are superior to even an unconstrained random algorithm, even in the face of significant exclusion areas.

3 ORIGINAL MWA LAYOUT

We have used our new algorithm to determine the originally planned 512-antenna layout of the MWA. The MWA is currently funded at the 128 antenna level, with the capacity to easily expand to 256 antennas given modest additional funding (Tingay et al. 2012). The original concept for the MWA was 512 antennas (Lonsdale et al. 2009), though expansion to 512 antennas will require significant additional investment in MWA infrastructure. In this work we assess the originally envisaged 512 antenna concept for the MWA, and the currently funded MWA will consist of a 128 antenna subset of the array presented here. We present an analysis of the as-funded MWA in Tingay et al. (2012), and its cosmological sensitivity in Beardsley et al. (2012).

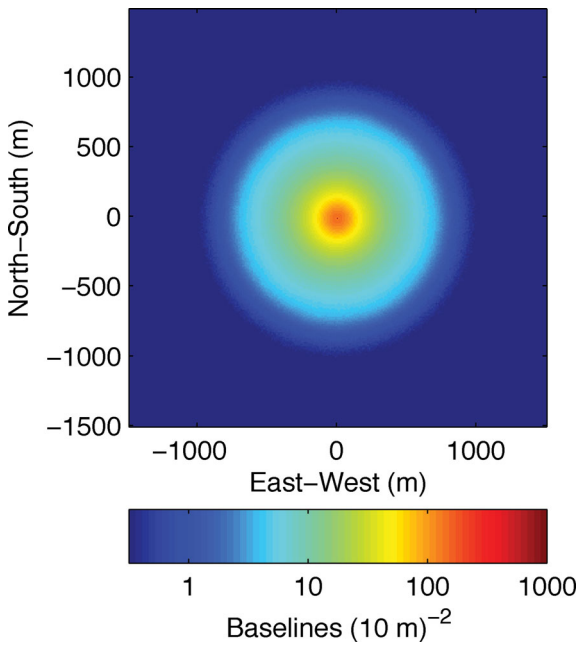

Figure 3. MWA ideal *uv* distribution. This distribution was used in the active masked method for generating the original MWA layout.

In our work, the majority of the 512 antennas (496) will be distributed over a 1.5-km diameter core, with the remaining 16 antennas at a ∼3-km diameter to provide higher angular resolution for solar measurements. The 16 'outliers' are placed by hand, while we implement our algorithm for the 496 core antennas. The antenna density distribution will be constant within a central 50-m radius, and have an r^{-2} dependence beyond (see Lonsdale et al. 2009, for a full description of the original concept for the MWA instrument, and Tingay et al. 2012 for a description of the as-funded MWA). The smooth ideal *uv* distribution is an autoconvolution of this antenna density distribution, and is shown in Fig. 3.

Several parameters of the algorithm were explored to further improve the quality of the arrays being generated. For example, we

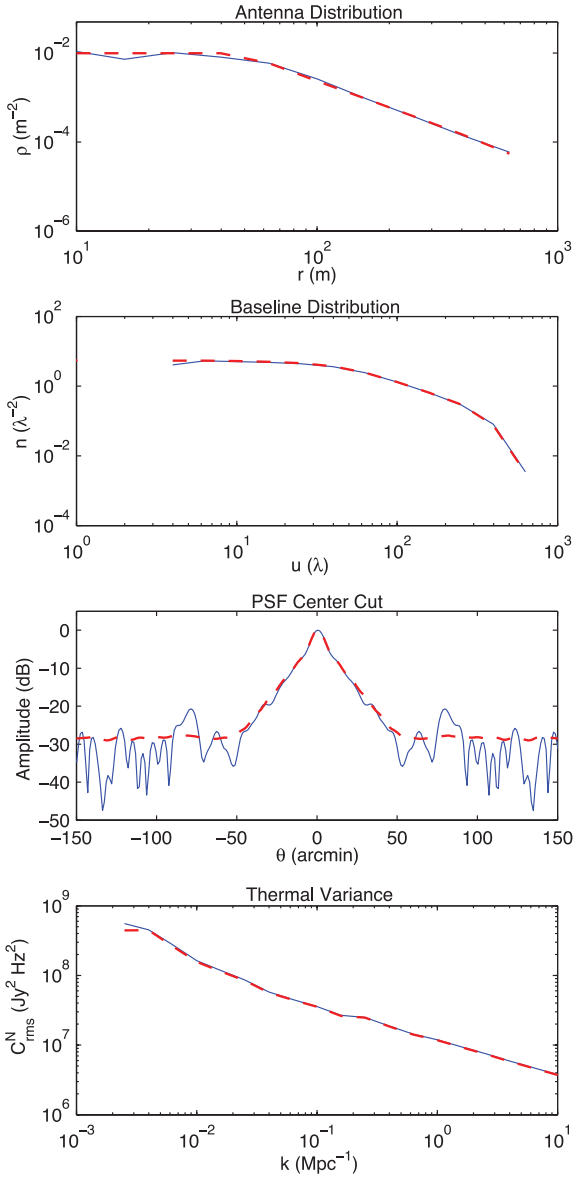

Figure 4. In each figure, the original MWA array layout (thin solid blue) is compared to the analytic ideal baseline distribution (thick dashed red) at 150-MHz observing frequency. Top to bottom: these are the radial antenna distribution, the radial baseline distribution, a cut through the snapshot single-frequency PSF and the thermal noise as a function of cosmological wavenumber k for a fiducial EoR measurement (following Bowman et al. 2006). In all aspects, the original array very nearly traces the ideal array.

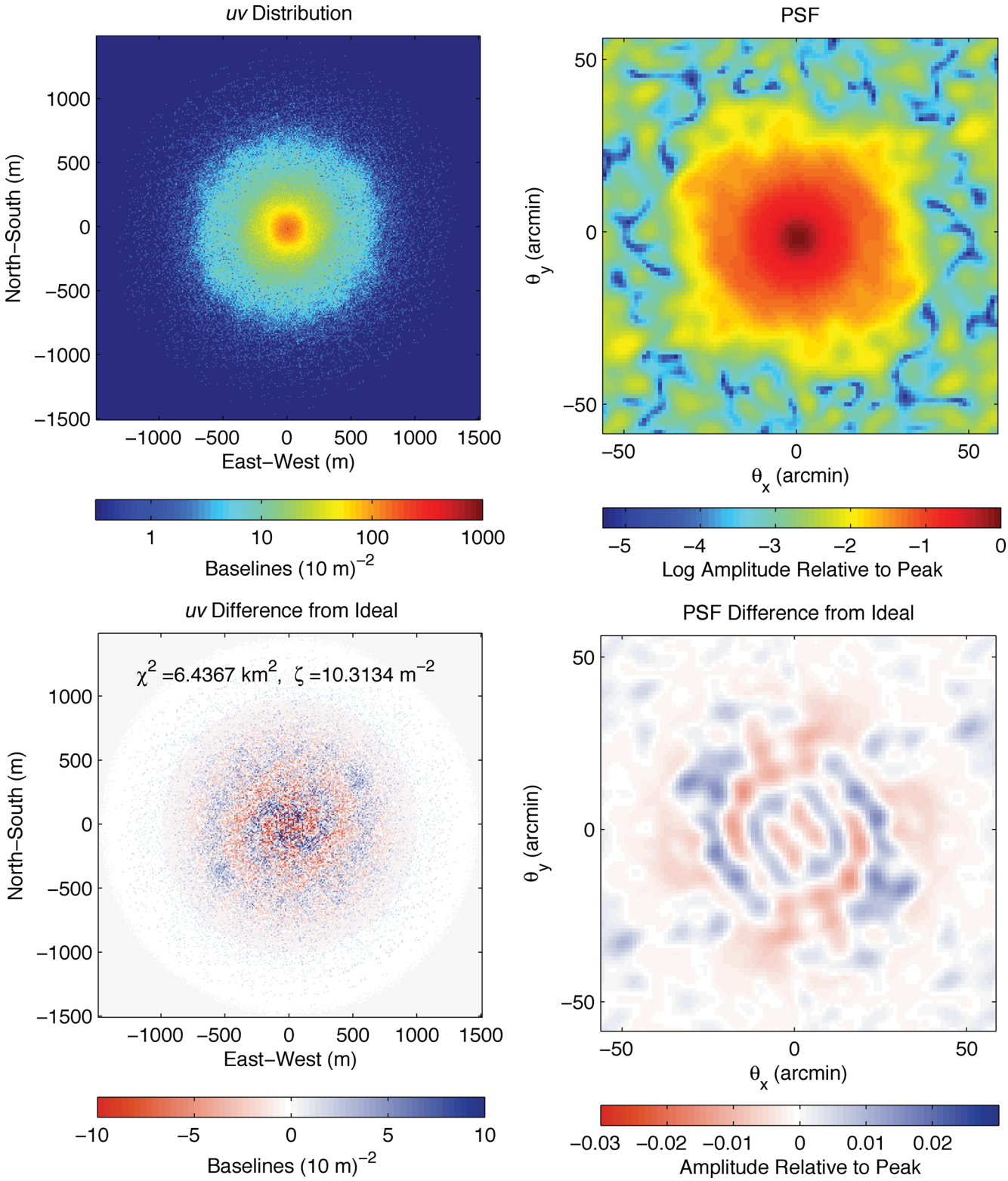

Figure 5. Baseline distribution and PSF of the original MWA array layout. The baseline distribution is shown in the left column, with the difference from ideal on the bottom. The azimuthal structure is nearly completely suppressed, and only small-scale noise remains. The snapshot PSF for 150 MHz at zenith is shown in the right column. The sensitivity relative to the peak is shown on the top, while the difference from ideal is on the bottom. The residual ripples in the PSF difference are ≈1 per cent of the peak, which is on order with the background ripples expected due to our finite number of antennas. Compare the top left-hand panel with Fig. 3.

varied the number of random antennas placed before initializing the active phase of our algorithm. We found that placing 350 random antennas (according to the ideal antenna distribution described above) provided sufficiently unconstrained initial conditions to proceed with the active phase. Running the algorithm in this mode 500 times provided a good sampling of the phase space.

We also investigated several array centre locations within a few hundred metres of the nominal array location. Due to the irregular distribution of avoidance areas on the ground, choosing different centres did have an effect on the quality of the best arrays generated by our algorithm. In particular, a centre near a high concentration of vegetation or rock outcrops usually results in a deficit of short baselines. We used this information, along with feedback from a ground truth survey in 2011 February to determine our final array centre.

After generating 500 candidate arrays for each potential location, we used ζ as a guideline for selecting the highest quality array layouts, backed by hand grading. The result is the final location and layout of the MWA. The locations of 496 core antennas, along with the 16 hand placed outliers, are available electronically (see Supporting Information). Figs 4 and 5 show the corresponding *uv* distribution and PSF. There is essentially no asymmetry in the final array – all of the large-scale structure is greatly suppressed, providing a very smooth *uv* sampling. The small residual ripples in the PSF are of the order of the background noise we expect due to the finite number of antennas. Following the discussion of Morales (2005) and using the parameters from Bowman et al. (2006), the thermal noise uncertainty on the EoR power spectrum can be calculated in the bottom panel of Fig. 4. With the exception of the small deviation at very low cosmological wavenumber, k, the thermal noise for our proposed layout very nearly traces that of the ideal array. Fig. 6 shows an illustration of the final array overlaid on an aerial photo of the site.

4 CONCLUSIONS

While we have been motivated by the need to explore array configurations for the MWA with exquisite smoothness in the PSF despite significant exclusion areas, we hope that our method will be useful for determining the antenna layouts of other large N arrays. In particular, we have developed a new figure of merit based on Bessel decomposition that is sensitive to large scale over- and underdensities in the *uv* plane. We have shown that algorithms based on this figure of merit can achieve extremely smooth baseline distributions while avoiding areas where antennas cannot be placed.

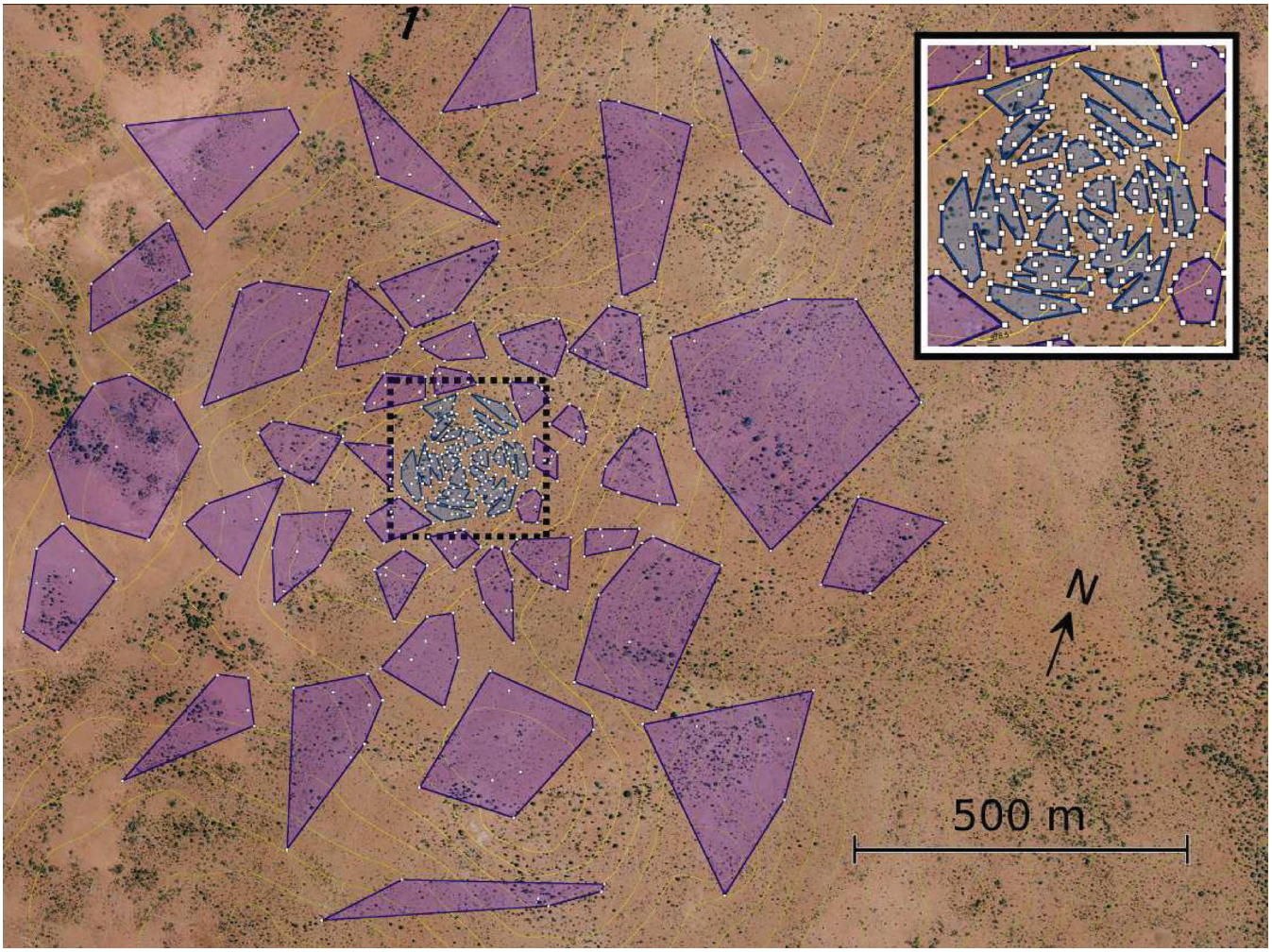

Figure 6. An aerial photograph of the MWA site with the original 496 antenna core array superimposed. White squares represent antennas (to scale). The coloured polygons depict a possible receiver scheme. Each polygon outlines a receiver set's electrical footprint (eight antennas per polygon except for a few outer receiver sets that will service some of the 16 outlier antennas not shown here). Inset: an enlarged view of the centre of the array.

Table A1. List of tile locations for 512 tile MWA layout. The locations listed are in metres east and north relative to the centre of the array at −26°42′4.″77521 latitude, 116°40′11.″39333 longitude. The first 496 tiles were placed using our algorithm described in the paper, while the final 16 tiles were placed by hand to optimize solar measurements. This is a sample of the full table, which is available as Supporting Information with the online version of the paper.

Tile number	East (m)	North (m)	Tile number	East (m)	North (m)	Tile number	East (m)	North (m)
0	58.39	175.52	54	102.43	21.22	108	162.64	199.62
1	−66.83	−117.18	55	622.87	317.32	109	35.21	48.62
2	4.47	−44.18	56	−153.15	82.42	110	12.78	−36.28
3	−22.48	27.72	57	58.24	−4.48	111	−65.47	−159.48
4	−139.89	−49.88	58	−8.72	77.52	112	−15.83	156.72
5	105.98	−16.38	59	46.77	−75.08	113	119.55	−3.68
6	275.71	−257.68	60	−375.14	−116.48	114	91.21	162.32
7	149.63	−188.58	61	−144.67	65.82	115	−9.19	−73.78
8	−589.30	−12.68	62	−6.06	−127.28	116	−45.47	79.32
9	−554.53	−344.68	63	299.67	−25.78	117	164.78	103.42
10	−235.98	−97.48	64	−85.48	203.32	118	9.21	43.42

We have used this new algorithm to generate a 512-antenna layout of the MWA. The first construction stage of the MWA will consist of a 128-antenna subsample of the array configuration shown in this paper.

Our figure of merit is similar, but different from the traditional approach of minimizing the maximum sidelobe. Both figures will result in low unwanted structure in the PSF. While minimizing the maximum sidelobe focuses on a hard constraint of the maximum peak, ζ captures a more holistic picture of the distribution with a softer constraint. Further work would be necessary to more precisely characterize the differences between the two.

Further work could also explore the possibility of implementing genetic algorithms or stimulated annealing with our figure of merit, ζ. For our present work, however, a trial-and-error method sufficed, and avoided questions of convergence while sampling a sufficient area of phase space.

ACKNOWLEDGMENTS

We acknowledge the Wajarri Yamatji people as the traditional owners of the Observatory site. We would like to particularly thank Angelica de Oliveira-Costa of Haystack Observatory for helpful conversations and feedback.

Support came from the U.S. National Science Foundation (grants AST CAREER-0847753, AST-0457585, AST-0908884 and PHY-0835713), the Australian Research Council (grants LE0775621 and LE0882938), the U.S. Air Force Office of Scientific Research (grant FA9550-0510247), the Smithsonian Astrophysical Observatory, the MIT School of Science, the Raman Research Institute, the Australian National University, the iVEC Petabyte Data Store, the Initiative in Innovative Computing and NVIDIA sponsored Center for Excellence at Harvard, and the International Centre for Radio Astronomy Research, a Joint Venture of Curtin University of Technology and The University of Western Australia, funded by the Western Australian State government.

REFERENCES

Beardsley A. P. et al., 2012, preprint, arXiv:1204.3111
Bernardi G., Mitchell D. A., Ord S. M., Greenhill L. J., Pindor B., Wayth R. B., Wyithe J. S. B., 2011, MNRAS, 413, 411
Boone F., 2001, A&A, 377, 368
Bowman J. D., Morales M. F., Hewitt J. N., 2006, ApJ, 638, 20
Cohanim B., Hewitt J., Weck O. D., 2010, ApJS, 154, 705
Cornwell T. J., 1988, IEEE Trans. Antennas Propagation, 36, 1165
Datta A., Bowman J., Carilli C., 2011, ApJ, 724, 526
Jackson J., 1999, Classical Electrodynamics. Wiley, New York
Kogan L., 2000, IEEE Trans. Antennas Propagation, 48, 1075
Kogan L., Cohen A., 2005, LWA Mem., 21
Liu A., Tegmark M., 2011, Phys. Rev. D, 83, 103006
Lonsdale C. et al., 2009, Proc. IEEE, 97, 1497
Morales M. F., 2005, ApJ, 619, 678
Morales M., Wyithe J., 2010, ARA&A, 48, 127
Morales M. F., Bowman J. D., Hewitt J. N., 2006, ApJ, 648, 767
Tingay S. J. et al., 2012, preprint, arXiv:1206.6945
Vedantham H., Shankar N. U., Subrahmanyan R., 2012, ApJ, 745, 176

APPENDIX A: TILE LOCATIONS

SUPPORTING INFORMATION

Additional Supporting Information may be found in the online version of this article:

Table A1. List of tile locations for 512 tile MWA layout.

Please note: Wiley-Blackwell are not responsible for the content or functionality of any supporting materials supplied by the authors. Any queries (other than missing material) should be directed to the corresponding author for the article.

This paper has been typeset from a TEX/LATEX file prepared by the author.